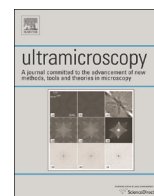




ELSEVIER

Contents lists available at ScienceDirect

Ultramicroscopy

journal homepage: www.elsevier.com/locate/ultramic

Surface effects on mean inner potentials studied using density functional theory

Robert S. Pennington^{a,*}, Chris B. Boothroyd^b, Rafal E. Dunin-Borkowski^b^a Institute for Experimental Physics, Ulm University, Albert-Einstein-Allee 11, 89081 Ulm, Germany^b Ernst Ruska-Centre and Peter Grünberg Institute, Forschungszentrum Jülich, 52425 Jülich, Germany

ARTICLE INFO

Article history:

Received 21 April 2015

Received in revised form

22 July 2015

Accepted 26 July 2015

Available online 29 July 2015

Keywords:

Electron holography

Mean inner potential

Surface reconstruction

Density functional theory

ABSTRACT

Quantitative materials characterization using electron holography frequently requires knowledge of the mean inner potential, but reported experimental mean inner potential measurements can vary widely. Using density functional theory, we have simulated the mean inner potential for materials with a range of different surface conditions and geometries. We use both “thin-film” and “nanowire” specimen geometries. We consider clean bulk-terminated surfaces with different facets and surface reconstructions using atom positions from both structural optimization and experimental data and we also consider surfaces both with and without adsorbates. We find that the mean inner potential is surface-dependent, with the strongest dependency on surface adsorbates. We discuss the outlook and perspective for future mean inner potential measurements.

© 2015 Elsevier B.V. All rights reserved.

1. Introduction

The amplitude and phase of the electron beam in the transmission electron microscope are directly accessible using electron holographic techniques [1–3]. The sensitivity of the electron phase to electric and magnetic potentials has been used for quantitative micro- and nano-scale materials characterization on a wide variety of specimens [4–10]. However, quantification of phase shifts inside material relative to free space relies on knowing the material's mean inner potential V_0 [3]. V_0 , defined as the mean electrostatic potential difference in a material relative to free space far from the material, is related to the zero-scattering-angle electron scattering factor and diamagnetic susceptibility [11,12,3]. For a single material, measurements of V_0 performed by different groups do not necessarily agree [13], so density functional theory (DFT) calculations have been used previously to attempt to predict V_0 [14]. Because an infinite crystal with no surfaces has no external reference point to use for an electrostatic potential and thus no definable mean inner potential [15], surfaces must be present for V_0 to be defined, but rarely has the effect of the surface been explicitly considered in these DFT calculations [16,17], especially systematically or explicitly.

Experimental V_0 measurements using off-axis electron holography started soon after the development of the electrostatic biprism [2], with attempts in the 1950s to measure V_0 for carbon

* Corresponding author.

E-mail address: robert.pennington@uni-ulm.de (R.S. Pennington).

[18], gold, and other materials [4]. Continued interest has led to electron holographic V_0 measurements for many materials, including semiconductors such as silicon [19–21,14], germanium [22] and group III–V materials [23,14]. Other non-holographic methods, such as electron diffraction, have also been used for mean inner potential determination on materials such as diamond, silicon, germanium, and metals [24–26].

However, as previously noted [26,14], these measurements often do not agree with each other, or have large margins of error. Kruse et al. [14] cite four compounds with more than one reported V_0 measurement (Si, Ge, GaAs, and InP), and, in all four cases, at least one measurement disagrees with the others. For germanium, an evaporation-based “wet” preparation determined 15.6 ± 0.8 V [27], and a cleaved (110) wedge found 14.3 ± 0.2 V [22]. For crystalline silicon, V_0 has been measured to be 9.26 ± 0.08 V from (111)-cleaved wedges [19], 12.1 ± 1.3 V from oxide-covered Si nanospheres [20], 11.5 ± 0.5 V from crushed bulk Si [21], and 12.52 ± 0.71 V from (110)-cleaved wedges [14]; we note that the first of these silicon values is much lower than the following three measurements. Even if only the latter three silicon values are considered, this provides a wide range of possible V_0 values with large margins of error. There are possible experimental explanations for these discrepancies, including dynamical diffraction [19,28] and anomalies for V_0 measurements of small nanoparticles were attributed to size-dependent strain [29], as well as specimen charging and inaccurate thickness determination. Thus, to establish V_0 benchmark values with higher precision, simulations have proven useful.

V_0 can be calculated from isolated-atom scattering factors

(IASF), or simulated using *ab initio* methods like density functional theory (DFT). The IASF approach has the advantage of being notably faster, simply requiring tabulated electron scattering factors [12,30] calculated for isolated atoms. However, IASF neglects chemical bonding, which has a notable effect [14]. DFT is more realistic, and includes chemical bonding, exchange, and correlation effects, but DFT exchange-correlation functionals also introduce some approximations [31]. DFT V_0 calculations previously reported include those of silicon, germanium, and MgO [16], wurtzite-structure group III–V semiconductors and gold [32], group II–VI semiconductors [33], zincblende-structure group-IV and group-III–V semiconductors [14], and multiple carbon allotropes (diamond, graphite, and amorphous carbon) [34].

Both different DFT programs, and different density functionals, can be used for V_0 simulation. In this work, we chose the GPAW code [35] because its use of grid-based projector-augmented wavefunctions in real-space [31,36] provides easy calculation of V_0 [17], and to compare with WIEN2k as used in [14]. We also use only the PBE (Perdew–Burke–Ernzerhof) exchange–correlation functional [37] to model electron–electron interactions, which is a common choice, including for V_0 calculation [14], but not the only choice (e.g. [16] uses the LDA (Local Density Approximation) exchange–correlation functional [31]). Different exchange–correlation functionals make different approximations for electron–electron interactions, and, thus, choosing a functional also chooses which approximations are made [31,37]; we discuss the effect of different functionals on V_0 in Appendix A.

Surface effects on electron-holographic measurements of V_0 have been briefly considered previously. Saldin and Spence in [38] discussed the theoretical influence of the Fermi level and the work function on V_0 . According to their formulation, changes to the work function should lead to changes in the mean inner potential. For DFT-simulated V_0 , Kim et al. [16] briefly consider the effect of different bulk-terminated surfaces, but for only a few cases. Our previous DFT simulation work, in [17], also considers only a few cases. This leads to the question of whether testing a range of surfaces and several materials in-depth would show a surface-dependent V_0 .

In this work, we consider the effect of the specimen surface on V_0 through DFT calculations for different specimen surface conditions, expanding on our previous work [17]. In Section 2, we present results from DFT simulation of the mean inner potential using the GPAW program [35], first determining what precision can be expected for V_0 simulations with GPAW, then testing “thin-film” cases for quantitative V_0 simulations and “nanowire” cases to further explore and explain the surface effects seen in the thin-film simulations. Finally, in Sections 3 and 4, we discuss these results, and provide some guidance for future mean inner potential measurements.

2. Results

In this section, we report the results of our DFT calculations of the mean inner potential (V_0). Our DFT simulations use the GPAW code [35] (version 0.6 stable) and its dependency, the Atomic Simulation Environment (version 3.2.0 stable) [39], and experimental lattice parameters are from the literature [40,41]. Generating V_0 requires summing the electrostatic potential over a volume. As previously reported [17], we sum the grid-based pseudo-Hartree electrostatic potential in that volume combined with the electrostatic-correction function’s set of scalars for each atom inside that volume, where the electrostatic corrections are calculated for the core electrons of each atom using the known PAW atomic setups and the unit-cell volume.

We use both “thin-film” and “nanowire” specimen geometries

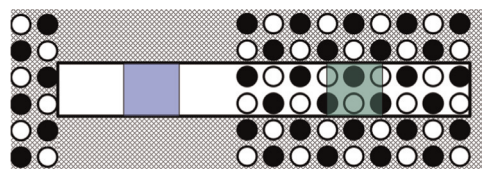


Fig. 1. Thin-film simulation geometry for a (110) surface, projected along the \hat{x} -axis. The black-outlined, non-crosshatched area is the specimen geometry input into the program, with both specimen and vacuum regions. The crosshatched area represents the effect of infinite periodic boundary conditions. V_0 is calculated by subtracting the average electrostatic potential over the middle unit cell of the specimen (green) from an equivalent volume in the middle of vacuum (blue). Note that the geometry seen here is also periodic in the direction normal to the page. (For interpretation of the references to color in this figure caption, the reader is referred to the web version of this paper.)

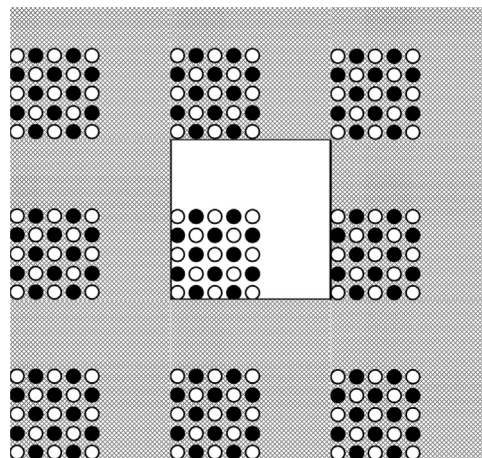


Fig. 2. Nanowire simulation geometry, projected along the \hat{x} -axis. As with Fig. 1, the crosshatched area represents the effect of periodic boundary conditions. The nanowires are infinitely long in the direction normal to the page.

in our simulations. Shown in Fig. 1, a “thin-film” specimen has surfaces in the \hat{z} direction, and material extending infinitely in the \hat{y} and \hat{x} directions, like an infinite thin film. This is the approach that has been reported previously for V_0 calculation. We also introduce a “nanowire” specimen, not previously reported. Shown in Fig. 2, a “nanowire” specimen has surfaces in the \hat{z} and \hat{y} directions, and material extending infinitely in the \hat{x} direction, like an infinitely long nanowire. In both cases, periodic boundary conditions are used in all three directions, so the thin-film simulation simulates an infinite stack of thin-films, and the nanowire simulation simulates an infinite array of nanowires. The distances between the surfaces of different objects are chosen to avoid interaction effects between different thin films or nanowires.

First, we discuss the accuracy and precision of V_0 simulated using our chosen DFT code, GPAW, and compare it to the WIEN2k code in [14]. However, we must then discuss DFT-generated minimum-energy lattice parameters. These sections establish a “baseline” for V_0 , using (110) bulk-terminated surfaces.

Second, we present the results for V_0 simulated from different surface states. For clean surfaces, we examine bulk-terminated and surface-reconstruction states, with surface reconstructions either from the literature or using DFT structural optimization. For surfaces with adsorbates, we consider first experimental adsorbate states, but we focus on structurally optimized adsorbate configurations. These specific adsorbate configurations are not necessarily experimentally achievable, but they are used to provide insight into surface effects on V_0 .

Third, to help explain the surface dependence we see, we present the results of “nanowire” simulations. The nanowire simulations display fringing fields, as expected, which helps explain

the surface dependence of the mean inner potential.

2.1. Accuracy and precision

In this section, we establish confidence intervals for our V_0 simulations. These DFT simulations have multiple tunable parameters that describe the DFT simulation volume and grid. We systematically vary each of those tunable simulation parameters to determine our simulations' precision, using thin-film specimen geometries of zincblende/diamond C, Si, Ge, and GaAs with bulk-terminated (110) surfaces. We then compare our DFT V_0 results against those reported previously, establishing how accurately our code determines V_0 , compared to other DFT codes.

For our GPAW simulations, four parameters are relevant: the number of reciprocal-space (Brillouin-zone) k -points, the spacing between real-space grid points (h), the width of vacuum around the thin-film (n_{vac}), and the thickness of the thin-film (n_{mat}). h is in nanometers; n_{vac} and n_{mat} are specified in units of the unit-cell width in the \hat{z} direction. Simulations on thin-film geometries use ($k \times k \times 1$) k -points, because different thin-films should be independent, and the k -point grid is along the same directions as the simulation grid. For reliable results, a whole number of grid points (h -points) per basic unit cell are necessary [17], which means that n_{vac} should be a multiple of the \hat{z} unit-cell width. h is also lattice-parameter-dependent and can be slightly different along different directions, because there must be a whole number of grid points spanning the simulation volume in each direction.

For precision testing, one parameter is varied over multiple simulations, and the other three parameters are set to the "standard" value. The standard k -point sampling used is $k=6$. The standard value of $n_{mat} = 7$ corresponds to 15 monolayers of material (*i.e.* the atomic positions lie on 15 different \hat{z} planes). The exact width is lattice-parameter-dependent, for example, 26.9 Å for silicon with lattice parameter $a=5.431$ Å. The standard value of $n_{vac} = 5$, also lattice-parameter-dependent, is 19.2 Å for silicon. The standard value of h used was $(h_C, h_{Si}, h_{Ge}, h_{GaAs}) = (0.1576, 0.1920, 0.1667, 0.1666)$ Å along the (110) direction for the reference lattice parameters, corresponding to (16, 20, 24, 24) grid points per unit cell along the (110) direction, respectively. These values were chosen to provide the minimum number of grid points consistent with keeping $h < 0.2$ Å, balancing accuracy and computational resources; finer grid spacings for the volume are more accurate but they use many more computational resources, and h is more relevant than the number of grid points because it already accounts for lattice-parameter differences.

Fig. 3 shows the full test-suite results for Si. If k , n_{mat} , or n_{vac} are too small, or h is too large, then the simulation may yield misleading results due to under-sampling or boundary effects. Conversely, increasing k , n_{mat} , or n_{vac} , or decreasing h , is computationally intensive. From these results, we determined that these parameters are well-behaved for $4 \leq k \leq 16$, $5 \leq n_{mat} \leq 14$, $2 \leq n_{vac} \leq 14$, and $0.2 \geq h \geq (0.08_C, 0.11_{Si,Ge,GaAs})$.

For each material, the standard deviation σ from the mean V_0 is determined for each parameter from the well-behaved simulations. The 2σ precision for each material is determined from adding in quadrature each parameter's σ for that material, then taking the square root, and doubling the result. The 2σ values for C, Si, Ge, and GaAs are shown in Table 1, and are used throughout this work for these materials. The average of these four 2σ values, 0.06 V, is taken as the error for any other materials.

We find that GPAW's V_0 simulation precisions compare favorably to the work done by Kruse et al. using the WIEN2k DFT code [14], although there are some differences. These error values are broadly comparable to the 0.03 V error found for V_0 DFT calculations using WIEN2k, although theirs is calculated differently, and so might not be precisely comparable. For them as for us, the thin-

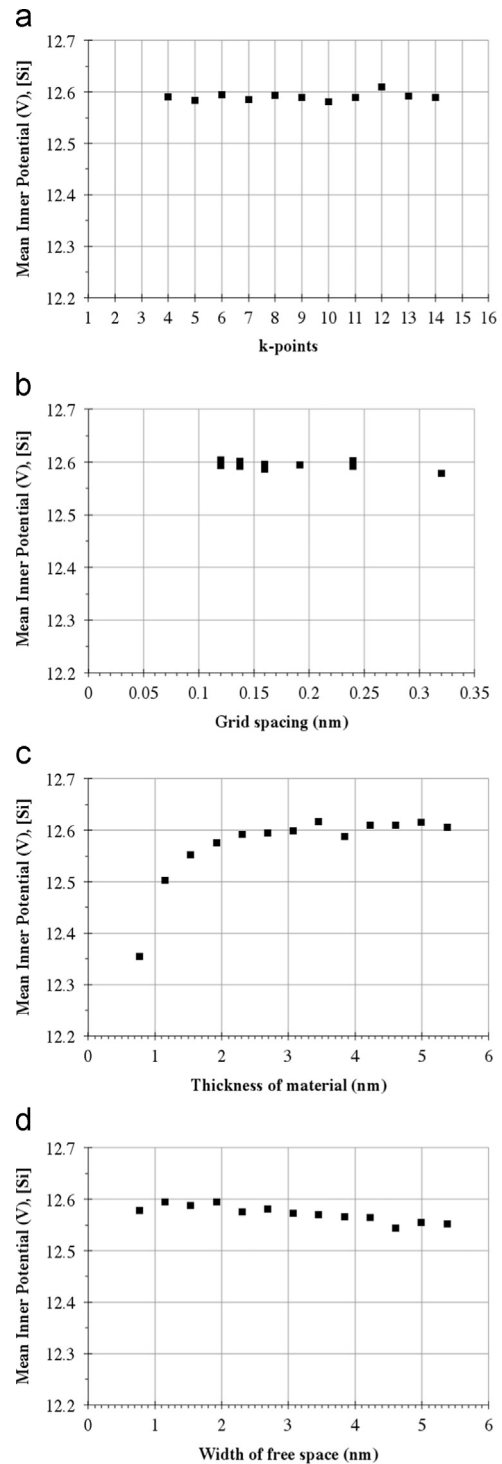


Fig. 3. Precision test results for Si. Multiple data points with the same h stem from changing the grid spacing in the directions orthogonal to the surface, and are included in the precision analysis if $h \leq 0.2$ Å.

film and vacuum widths were the largest single sources of error. Many of their WIEN2k-specific sources of error are not relevant for this work due to the nature of the GPAW real-space code. We include parameters that are less precise than the "standard" value we use, while they determine their error only from parameters more precise than their converged value. Considering these factors, for V_0 simulations, GPAW is comparably precise to WIEN2k as used by Kruse et al. [14].

Some of the behavior seen in Fig. 3 helps illustrate the

importance of determining 2σ values. While Fig. 3d shows that V_0 decreases slowly for increasing n_{vac} , this decrease is small (about 0.01 V/nm of n_{vac} increase), and is included in our error estimates. This should not affect different simulations run with the same n_{vac} , like we do in the following sections for (110)-type simulations. It may be a small effect on our simulations using different crystal facets, but this effect would be much smaller than the margin of error, and the different crystal-facet simulations are using similar n_{vac} spacings to the (110) simulations, so the same margin of error should still be valid. A full exploration of this effect would involve running many very large simulations, and this effect is so small that it is not possible to determine the cause from these simulations; thus, a full exploration is outside the scope of this work. Asymptotically decreasing interlayer coupling (*i.e.* insufficient spacing between layers) would be one possible explanation; however, the effect occurred for all the simulated materials, with no clear material dependence. Thus, it is perhaps more likely to be just an artifact of very large n_{vac} regions, where there are real-space grid points but no atoms. This effect is one reason why comprehensive margin-of-error simulations should be performed for comparison, and why a single good configuration should be established as a basis for comparison.

Our chosen DFT code yields similar V_0 values to those reported previously for a range of group-IV and group-III–V materials. Table 2 shows our DFT mean inner potential results ($V_{0,GPAW}$) compared with literature reports of DFT-simulated mean inner potentials ($V_{0,DFT}$) and the mean inner potential using isolated-atom scattering factors ($V_{0,IASF}$). The IASF mean inner potentials are much greater than the DFT results in all cases. In comparison, our DFT results are close to previously reported DFT results, with the exception of GaP which is about 3% lower. This is because Kruse et al. [14] use a GaP lattice parameter of 5.449 Å, while we use a larger one listed in the CRC Handbook of Chemistry and Physics [40]. Rescaling our result by the unit-cell volume (see the next section for details, especially Table 4) would yield a comparable MIP of 13.58 V, very close to the Kruse et al. value of 13.63 V.

Table 1

2σ values (in V) for C, Si, Ge, and GaAs, using the well-behaved parameter space described in the text. Reference lattice parameters a_r used were 3.567, 5.431, 5.658, and 5.653 Å, respectively, from the literature [40,41]. The Ge $k=14$ simulation failed to run, and is not included.

$(a = a_r)$	k	h	n_{mat}	n_{vac}	Total 2σ
C	0.013	0.008	0.013	0.016	0.051
Si	0.008	0.006	0.013	0.017	0.047
Ge	0.012	0.005	0.035	0.017	0.082
GaAs	0.008	0.017	0.019	0.023	0.071

Table 2

Simulated V_0 (in V) for group-IV and group-III–V materials. $V_{0,GPAW}$ is this work, $V_{0,DFT}$ is other literature reports using DFT, $V_{0,IASF}$ is from isolated-atom scattering factors. Reference lattice parameters a_r used were from the literature [40,41]. Isolated-atom scattering factors (IASF) are from Rez et al. [30].

$(a = a_r)$	$V_{0,GPAW}$	$V_{0,DFT}$	$V_{0,IASF}$
C	20.36 ± 0.05	20.33 [34]	20.86
Si	12.59 ± 0.05	12.57 [14], 12.42 ± 0.09 [16]	13.76
Ge	14.73 ± 0.08	14.67 [14]	15.60
GaAs	14.18 ± 0.07	14.19 ± 0.03 [14]	15.38
InP	13.87 ± 0.06	13.90 [14]	15.22
InAs	14.18 ± 0.06	14.34 [14]	15.47
GaP	13.28 ± 0.06	13.63 [14]	14.60
AlP	11.46 ± 0.06	11.39 [14]	13.41
AlAs	12.35 ± 0.06	12.34 [14]	13.97

In this section, we have established that the GPAW DFT code generates mean inner potentials comparable to those reported previously. We have also established the precision of our DFT code. However, before we discuss simulations involving different surface structures, we first must discuss DFT minimum-energy lattice parameters.

2.2. Lattice parameters

The minimum-energy lattice parameter generated using DFT (a_d) is known to not match experimental lattice parameters (a_r), and this mismatch is dependent on which approximations are made, including the density functional, as been noted previously for the WIEN2k code [42] and for GPAW [35]. As discussed above, the density functionals used are approximations for electron–electron interactions. The effect of the minimum-energy lattice parameter on V_0 has been considered for the WIEN2k code [33], which we discuss later in this section as a comparison. The minimum-energy lattice parameter is required in this work when performing structural optimizations, to avoid constructing pre-strained systems.

We must use minimum-energy lattice parameters for our structural optimization simulations. During structural optimization, atomic positions shift to minimize the forces on each atom, but the simulation cell remains constant. Thus, the atoms in the simulation will want to be their optimal distance apart – which is not the same as the experimental interatomic distances if $a_d \neq a_r$ – so any optimization should start with these minimum-energy distances. Additionally, the fixed simulation cell with its periodic boundary conditions effectively distorts the crystal if the simulation cell does not correspond to the minimum-energy lattice parameter, because the interatomic distances are pinned by the periodic boundary conditions. This would act like strain – for example, for a thin-film simulation, the crystal unit cells' in-plane distances are fixed by the periodic boundary conditions, but only the out-of-plane distance could relax due to the large vacuum region. The minimum-energy lattice parameters are calculated using built-in GPAW functions designed for this. Therefore, we used minimum-energy lattice parameters for any simulation that included structural optimization (except diamond C, as discussed below).

Table 3 shows the GPAW minimum-energy lattice parameters a_d for the materials with mean inner potentials listed in Table 2. For all of these materials, $a_d > a_r$, by +0.28% to +2.12%. However, according to the isolated-atom scattering factor model, the mean inner potential scales inversely with unit cell volume (a^3) [12]. For these materials, $(a_d)^3 > (a_r)^3$ by +0.84% to +6.50%. As discussed above, this is expected behavior that has been observed for multiple DFT programs.

Due to the unit-cell-volume change, we expect that V_0 should

Table 3

Minimum-energy lattice parameters a_d calculated using GPAW. Reference lattice parameters a_r are experimental measurements from the literature [40,41]. Δa is the percent change in the lattice parameter; ΔVol is the percent change in the unit cell volume, and thus the approximate expected shift in V_0 from the IASF model.

Material	a_r (Å)	a_d (Å)	Δa (%)	ΔVol (%)
C	3.567	3.577	+0.28	+0.84
InP	5.869	5.908	+0.66	+2.01
InAs	6.059	6.100	+0.68	+2.04
Si	5.431	5.477	+0.85	+2.56
GaP	5.490	5.545	+1.00	+3.04
AlP	5.451	5.513	+1.14	+3.45
AlAs	5.662	5.740	+1.38	+4.19
Ge	5.658	5.765	+1.89	+5.78
GaAs	5.653	5.773	+2.12	+6.50

Table 4

Simulated V_0 (in V) for group-IV and group-III–V materials, using minimum-energy lattice parameters a_d , shown in Table 3. Precisions for each material were calculated using the full test suite detailed in Section 2.1 with a_d instead of a_r . “Error” is the imprecision in V_0 according to the test suite for each material, expressed as a percentage of V_0 . The last column, V.C.C., is the volume-compensated change in V_0 , determined by multiplying the mean inner potential by the unit-cell volume, i.e. $\Delta(V_0 \times a^3)$.

($a = a_d$)	$V_{0,\text{GPAW}}$ (V)	Error (%)	V.C.C. (%)
C	20.23 ± 0.04	(± 0.2)	+0.2
Si	12.32 ± 0.05	(± 0.4)	+0.3
Ge	13.88 ± 0.07	(± 0.5)	−0.3
GaAs	13.27 ± 0.08	(± 0.6)	−0.3

shift. Table 4 shows V_0 calculated using a_d , confirming this shift. The margins of error in Table 4 are calculated for mean inner potentials using the a_d lattice parameter in the same way as for those using a_r in Table 2. Because the final V.C.C. column is smaller than or equal to the error column, mean inner potentials calculated using a_d lattice parameters are only different due to the change in unit-cell volume (within the margin of error). This is also consistent with the findings for the WIEN2k code [33]. Thus, this V_0 shift is accounted for by the change in unit cell volume, and thus using the a_d lattice parameters instead of the a_r ones will lead to different V_0 values, but the trends should remain the same. However, as noted above, for structural optimizations, we use a_d to avoid building strain into our systems.

Which lattice parameter is appropriate depends on which DFT simulations are being run, and for what purpose. If the simulation does not involve structural optimization, then experimental lattice parameters (a_r) should be used, for easy comparison with experimental V_0 . The previous studies using the WIEN2k code [33] did not involve structural optimization, and thus, could choose to use only experimental lattice parameters. However, if the simulation does involve structural optimization, then minimum-energy lattice parameters (a_d) should be used for accuracy and internal consistency. The shifts in lattice parameter seen here are small, and the effect of scaling the unit cell on non-structurally optimized V_0 simulations are accounted for by volume effects, so V_0 calculated using a_d can be scaled by the unit-cell volumes into V_0 values for a_r -based experimental comparisons.

Therefore, to avoid building strain into the structural optimizations, any structural optimization simulation we run (with one exception) uses the a_d lattice parameter. For internal consistency, the shifts in V_0 seen under structural optimization are compared against a V_0 baseline using the a_d lattice parameter. This approach, required due to the structural optimizations, is internally consistent, but does require that any V_0 calculated using a_d would need to be scaled by the unit-cell volume for comparison with experiment. There is one exception, diamond C, where we test with both the a_d and a_r lattice parameters, because Δa and ΔVol are both small ($<1\%$). Throughout this work, the lattice parameter used (either a_r or a_d) is mentioned.

2.3. Surface-state simulations

Having established the baselines for (110) bulk-terminated mean inner potentials in the previous sections, we now discuss the effect on V_0 from changing the surface state of a thin-film simulation. We use the V_0 error estimates discussed in the previous sections to determine whether a given surface modification produces a shift in the mean inner potential relative to this baseline. We emphasize that, as shown in Fig. 1, the two simulation volume segments being subtracted to generate V_0 are far from the surfaces, so, in our simulations, a V_0 shift from surface modification is the

Table 5

V_0 for different group-IV bulk-terminated surfaces using experimental lattice parameters (a_r) and DFT minimum-energy lattice parameters (a_d). $\Delta_{(110)}$ (V) is the V_0 shift from the baseline (110) bulk-terminated value, and is boldfaced if outside the mutual margin of error.

Material	a	Facet	V_0 (V)	$\Delta_{(110)}$ (V)
C	a_r	(001)	21.41 ± 0.05	+ 1.05
	a_r	(111)	21.18 ± 0.05	+ 0.82
	a_r	(211)	20.75 ± 0.05	+ 0.39
Si	a_r	(001)	12.90 ± 0.05	+ 0.31
	a_r	(111)	12.65 ± 0.05	+0.06
	a_r	(211)	12.57 ± 0.05	−0.02
Ge	a_r	(001)	15.03 ± 0.08	+ 0.30
	a_r	(111)	14.77 ± 0.08	+0.04
	a_r	(211)	14.67 ± 0.08	−0.06
C	a_d	(001)	21.26 ± 0.04	+ 1.04
	a_d	(111)	21.04 ± 0.04	+ 0.82
	a_d	(211)	20.62 ± 0.04	+ 0.39
Si	a_d	(001)	12.85 ± 0.05	+ 0.54
	a_d	(111)	12.37 ± 0.05	+0.06
	a_d	(211)	12.29 ± 0.05	−0.03
Ge	a_d	(001)	14.17 ± 0.07	+ 0.30
	a_d	(111)	13.81 ± 0.07	−0.07
	a_d	(211)	13.83 ± 0.07	−0.05

shift that would be expected in the bulk V_0 . We first consider bulk-terminated clean surfaces, followed by clean-surface reconstructions using reference atom positions or structural optimization. Then, we consider surface adsorbates.

2.3.1. Bulk-terminated clean surfaces

Bulk-terminated clean surfaces are the simplest surface-dependent case, where the atomic positions at the surface are the same as the bulk. While it is unrealistic to assume a real specimen would have a bulk-terminated clean surface, V_0 surface dependence in DFT simulations of bulk-terminated clean-surface specimens is a strong indication of a possible general mean inner potential surface dependence.

Table 5 shows V_0 calculated using bulk-terminated surface facets of (001), (111) and (211) for diamond C, Si, and Ge, respectively. All surfaces have atoms in the same positions on both the top and bottom surfaces. The $\Delta_{(110)}$ figure shows the shift (in volts) from the (110) “baseline” case, and is boldfaced if outside the mutual margin of error. For all three surfaces, V_0 of diamond C shifts outside the margin of error. Notably, the V_0 of diamond C (001) and C(111) are both greater than the IASF value (20.86 V) in Table 2. Si has the same V_0 for (110), (111), and (211), but a different V_0 for (001); the same is also true for Ge. The two lattice parameters (experimental a_r and DFT minimum-energy a_d) yield similar shifts in V_0 , with the exception of Si(001), for unknown reasons.

In short, Table 5 predicts that, for clean bulk-terminated surfaces, some materials would have surface-dependent mean inner potentials in their bulk, far from their surfaces. Clean-bulk-terminated surfaces on infinite thin films are not realistic specimens, but they establish that, when performing realistic electronic-structure calculations, the mean inner potential is surface dependent. This is in contrast to V_0 calculations using isolated-atom scattering factors, which include no chemical bonding and are orientation-independent. This is conceptually examined in greater detail in Section 3. Now, we present the effect of clean, reconstructed surfaces, including atomic rearrangement.

2.3.2. Reconstructed clean surfaces

Now, we proceed from clean, bulk-terminated surfaces to clean,

Table 6

V_0 for group-IV and group-III–V materials with reconstructed surfaces. a is lattice parameter used. Structural optimization uses force minimization, with the default convergence threshold $F < 0.05$ eV/Å [39]. “Facet” is the surface facet used, prefixed with “S” to indicate structural optimization, or “LR” to indicate a literature reference (see footnotes). Unless otherwise indicated, a (1×1) symmetry was used. $\Delta_{(110)}$ (V) is the V_0 shift from the baseline (110) bulk-terminated value, and is boldfaced if this value is outside the mutual margin of error.

Material	a	Facet	V_0 (V)	$\Delta_{(110)}$ (V)
C	a_r	S(110)	19.79 ± 0.05	− 0.57
	a_r	S(001)	21.42 ± 0.05	+ 1.06
	a_r	LR ^a	21.40 ± 0.05	+ 1.04
C	a_d	S(110)	19.72 ± 0.04	− 0.50
	a_d	S(001)	21.27 ± 0.04	+ 1.05
Si	a_d	S(110)	12.16 ± 0.05	− 0.15
	a_d	S(001)	12.90 ± 0.05	+ 0.59
	a_d	LR ^b	12.02 ± 0.05	− 0.30
	a_d	LR ^c	12.14 ± 0.05	− 0.18
Ge	a_d	S(110)	13.90 ± 0.07	+0.03
GaAs	a_d	S(110)	13.28 ± 0.08	+0.01
InP	a_d	S(110)	13.92 ± 0.06	+ 0.34
InAs	a_d	S(110)	14.09 ± 0.06	+ 0.18
GaP	a_d	S(110)	13.08 ± 0.06	+ 0.17
AlP	a_d	S(110)	11.58 ± 0.06	+ 0.47
AlAs	a_d	S(110)	12.10 ± 0.06	+ 0.25

^a (001)(2 × 1) relaxed reconstruction using reference symmetry from [43,44].

^b (001)(2 × 1) unrelaxed reconstruction using reference atom positions from [45].

^c As footnote b in this table, but relaxed using reference atom positions as starting values.

reconstructed surfaces. We consider the effect on V_0 of both selected experimentally determined reconstructions and structural optimizations [39].

Experimental surface reconstructions are more experimentally relevant than structural optimizations, in principle. However, due to computational constraints, only (2×1) or (1×1) reconstructions were feasible, and relatively few small-unit-cell surface reconstructions have reported full atomic positions. In addition, the surface atoms on a TEM sample could have non-equilibrium or dynamic atomic positions, due to e.g. the high-energy electron beam or contamination. In contrast, structural-optimization-determined atom positions are internally consistent with the DFT-determined electronic structure, analogous to minimum-energy lattice parameters. Thus, we performed some simulations using experimental surface reconstructions, but focused more on structural optimizations.

Table 6 contains V_0 values for thin-films with clean, reconstructed surfaces. We reiterate that the baseline V_0 value depicted in our tables is the (110) surface for that material and lattice parameter, not that particular bulk-terminated surface facet, because (110) surfaces are usually used for V_0 simulations. Of the two experimental cases, Si(001)(2 × 1) with full experimental atomic positions shows a V_0 shift relative to both (110) and (001) surfaces, while C (001)(2 × 1), whose experimental information is limited to just symmetry information, does not shift relative to the bulk-terminated (001) surface, but does relative to the bulk-terminated (110) surface (the baseline case). The Si(001)(2 × 1) simulation uses atomic positions scaled to the a_d lattice parameter; we reported previously that using the experimental lattice parameter yields $V_0 = 12.32$ V (for a V_0 shift of −0.27 V), under slightly different GPAW simulation conditions (i.e. $(8 \times 8 \times 1)$ k -points instead of $(6 \times 6 \times 1)$) [17]. However, as discussed elsewhere in this paper, this particular surface condition may not be easily experimentally accessible or stable in the TEM. In short, a surface condition derived from experimental data can have a V_0 shift relative to its respective bulk-terminated surface, or other bulk-terminated

surfaces.

In many cases, surface reconstruction with structural optimization leads to a V_0 shift relative to the same surface when bulk-terminated, but not for C(001)(1 × 1) or (2×1) , Ge(110) or GaAs (110), and possibly not Si(001)(1 × 1), although Si(001)(2 × 1) does show a V_0 shift relative to bulk-terminated Si(001). For (110)(1 × 1) surfaces with structural optimization, C, Si, InP, InAs, GaP, AlP, and AlAs all show a V_0 shift ranging from −0.57 V to +0.47 V. Thus, structural optimization can lead to a mean inner potential shift, but it is both facet- and material-dependent; under structural optimization, diamond C V_0 shifts for (110) surfaces but not (001).

From these results, we can conclude that surface atom rearrangement on clean surfaces makes a difference to the mean inner potential for some materials and some surfaces. However, due to contamination, real specimens may not have clean surfaces, as we discuss in the next section.

2.3.3. Adsorbates

In this section, we consider V_0 shifts from different adsorbate terminations of specimen surfaces. If a specimen is loaded from air into a non-ultra-high-vacuum TEM, it is not unreasonable to assume that some adsorbates may be on the specimen surface. We reiterate that our mean inner potentials are calculated from the two highlighted regions in Fig. 1, and those regions do not include surface atoms. Thus, our V_0 shifts are the shifts in the V_0 of the bulk material due to surface condition changes.

In all but one case, our adsorbate simulations involved structural optimization. One experimental set of atomic positions (Si(H/H), shown as “LR” [46]) was tested both using the experimental atom positions (LR^d) rescaled to the a_d lattice parameter, and using the experimental atom positions as a starting point, then structurally optimizing using force-minimization (LR^e). Our other adsorbate surfaces were constructed using a two-step process. In the first step, we took the clean, bulk-terminated thin film and replaced each atom in the top and bottom planes with adsorbate atoms. In the second step, we optimized the structure using force-minimization, with the default convergence threshold $F < 0.05$ eV/Å [39].

Table 7 shows the results of V_0 simulated for thin films with adsorbates, mostly for (110) surfaces. In every instance, adding a surface adsorbate shifts the mean inner potential. Using experimental atom positions, the mean inner potential of Si(001)(2 × 1)(H) shifts relative to the clean Si(001)(2 × 1) reconstructed surface in Table 6 by −0.50 V, or about 4%. Thin-films with hydrogen termination see their mean inner potentials decrease – for diamond C, by about 20%. Oxygen-termination increases the mean inner potential – for diamond C, by about 10%, and for Si, by about 28%. Replacing group-IV materials with other group-IV materials can either increase or decrease the mean inner potential. Taking a diamond thin-film and hydrogen-terminating the top surface and oxygen-terminating the bottom surface gives a mean inner potential between both-hydrogen-terminated and both-oxygen-terminated. In summary, the V_0 shift from surface adsorbates depends on both the material and the adsorbate.

Our objective is not to propose these surface structures as typical TEM specimen surfaces. However, we use these configurations to provide a consistent baseline to evaluate the effect of surface adsorbates on V_0 . The surface configurations detailed in this section may not be realistic for a TEM specimen, because electron beam damage may dynamically reconstruct the specimen surface, and lead to a non-equilibrium surface condition, or multiple surface layers. Our 1:1 hydrogen termination or 1:1 group-IV/group-IV termination may be more plausible than our 1:1 oxygen termination, because, for consistency, these 1:1 terminations are based on replacing surface atoms 1:1 with adsorbate atoms, and

Table 7

V_0 for group-IV and group-III–V materials with adsorbate-terminated surfaces. “Mat.(T/B)” is the bulk material, the top-surface adsorbate, and the bottom-surface adsorbate, respectively. All thin films except LR^d and LR^e have (110) surfaces (see footnotes). a is lattice parameter used. All scenarios except LR^d use structural optimization. $\Delta_{(110)}$ (V) is the V_0 shift from the baseline (110) bulk-terminated value, and is boldfaced if this value is outside the mutual margin of error.

Mat. (T/B)	a	V_0 (V)	$\Delta_{(110)}$ (V)
LR ^d	a_d	11.52 ± 0.05	−0.80
LR ^e	a_d	11.52 ± 0.05	−0.80
C(H/H)	a_r	16.20 ± 0.05	−4.16
C(O/O)	a_r	22.29 ± 0.05	+1.93
C(H/H)	a_d	16.12 ± 0.04	−4.01
C(O/O)	a_d	22.19 ± 0.04	+1.96
C(Si/Si)	a_d	19.42 ± 0.04	−0.81
C(H/O)	a_d	18.96 ± 0.04	−1.27
Si(H/H)	a_d	11.33 ± 0.05	−0.99
Si(O/O)	a_d	15.73 ± 0.05	+3.41
Si(C/C)	a_d	11.86 ± 0.05	−0.46
Si(Ge/Ge)	a_d	12.83 ± 0.05	+0.51
Ge(H/H)	a_d	12.38 ± 0.07	−1.50
Ge(C/C)	a_d	13.62 ± 0.07	+0.26
InAs(H/H)	a_d	12.97 ± 0.06	−0.94
InAs(O/O)	a_d	15.90 ± 0.06	+1.99

^d Si(H/H) (001)(2 × 1) reconstruction using reference atom positions from [46] rescaled to the a_d lattice parameter, without structural optimization.

^e As footnote d in this table, but structurally optimized using reference atom positions as starting values.

thus our oxygen termination places atomic oxygen, not molecular oxygen, onto the surface. In addition, Si(001)(2 × 1) (H) simulated with structural optimization and experimental atom positions both have the same V_0 , so structural optimization may provide useful structures.

In short, adsorbates strongly influenced the mean inner potential for all thin-film configurations studied. Adsorbate-based simulations may be useful for understanding the mean inner potential. In the next section, we consider the fringing fields outside “nanowire” geometries with multiple surface facets in the same simulation.

2.4. “Nanowire” simulations: fringing fields

As shown above, V_0 DFT simulations show V_0 to be surface-facet dependent. The above simulations are for infinite thin films with only one kind of surface facet in each simulation, as shown in Fig. 1. However, if multiple kinds of surface facets are present, do fringing fields, or some other mechanism, resolve the V_0 shift between surfaces? Is the V_0 shift between surfaces the same as that predicted by the thin-film simulations?

To explore this effect, we simulate “nanowires” that include two kinds of surface facets in the same simulation, as illustrated in Fig. 2. In this section, we explore this effect using three simulations. First, we present one bulk-terminated simulation with different nanowire facets (C(001) and C(110)), expected to show a V_0 shift between surfaces. Table 5 predicts a 1.05 V shift between bulk-terminated C(001) and bulk-terminated C(110). Second, we present one bulk-terminated simulation with the same nanowire facets (C(110) and C(1 $\bar{1}$ 0)), expected to not show a V_0 shift between surfaces. Third, we present the results from structurally optimizing the second simulation. Our nanowire simulations use diamond C due to its smaller lattice parameter and large surface-facet V_0 shift. The smaller diamond C lattice parameter allowed us to simulate more atomic layers within the same computational-constraint-limited volume. These nanowire configurations may not be experimentally feasible nanowires, but allow us to study the effect of

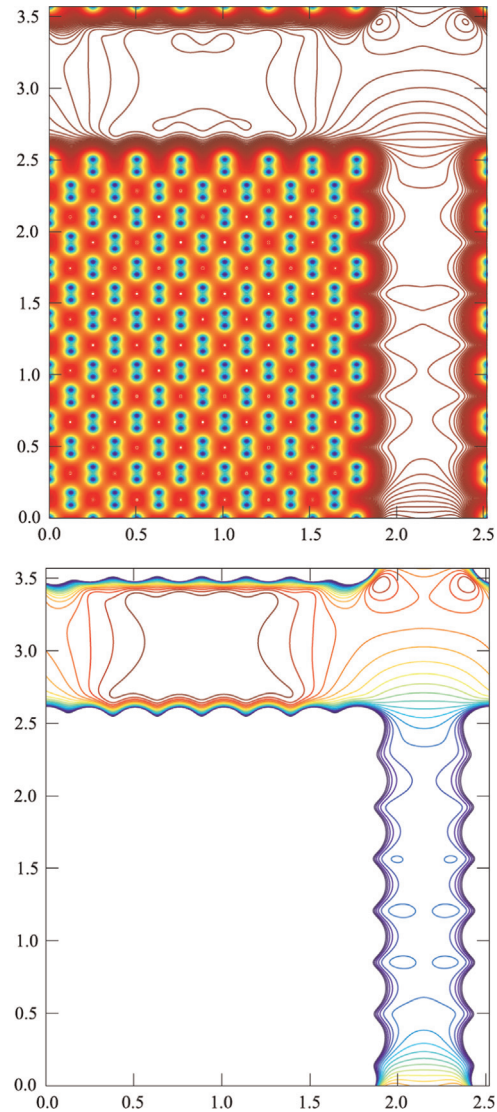


Fig. 4. Electrostatic equipotential contour maps from nanowire simulation of bulk-terminated C(001)/C(110) (top-bottom/left-right) using the GPAW pseudo-Hartree potential (V_{Hfg}), from one unit cell averaged along the long axis of the nanowire, in the geometry shown in Fig. 2. Equipotential contours every 0.1 V (from blue to red); x/y scale in nm. Top: equipotential contour map of the full potential range (starting at the bottom); solid-looking colored regions are due to very-close-together contours. Bottom: same volume, but equipotential contour map of only the top 2.0 V. The two (001) surfaces have different fringing fields because they are different cuts through the unit cell. The contours are in different locations because the two images have different contour reference points. (For interpretation of the references to color in this figure caption, the reader is referred to the web version of this paper.)

multiple surface facets on the mean inner potential. Analogous to the thin-film simulations, these nanowire simulations use ($k \times 1 \times 1$) k -points.

Fig. 4 shows equipotential contour plots from a nanowire with C(001) and C(110) facets, using the GPAW pseudo-Hartree electrostatic potential, which is quantitatively accurate for the fringing fields. As noted in the figure caption, the two (001) surfaces (top and bottom) are different cuts through the unit cell, and thus have slightly different fringing fields; the differences in contour location between the top and bottom images in Fig. 4 are due to different contour reference points. The top image of the entire electrostatic potential range shows the atomic positions and the fringing fields surrounding the wire; inside the nanowire, the contours are very close to each other, leading to the appearance of constant color.

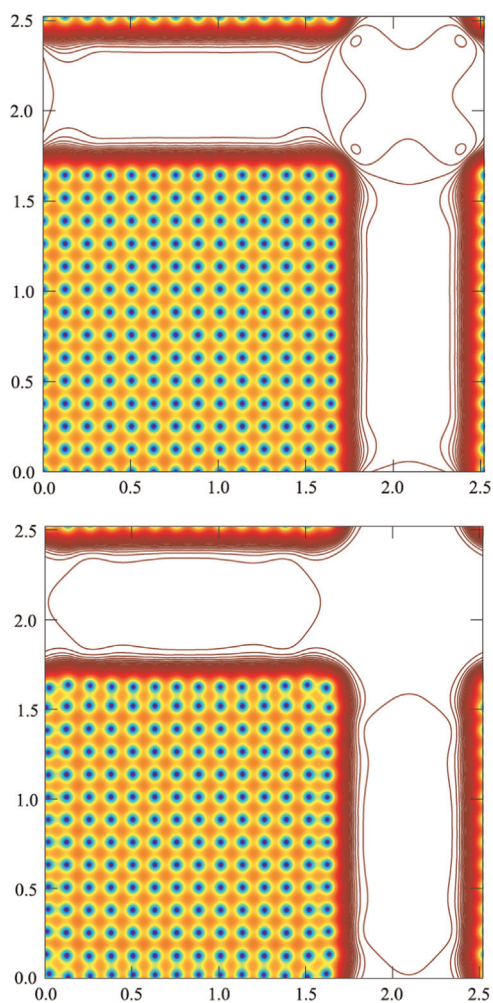


Fig. 5. Top: as top image in Fig. 4, but with bulk-terminated C(110)/C(110). Bottom: as top image, but with a structurally optimized atomic configuration.

These fringing fields are highlighted in the bottom image, which only graphs the top 2.0 V, and shows that the (001) facet's potential in vacuum is approximately 1.5 V greater than that of the (110) facet. This is larger than the +1.05 V predicted from the thin-film simulations, and is discussed further in the next section. However, the simulation volume may not be large enough to provide a fully converged potential in vacuum, due to computational constraints.

Fig. 5 shows the second and third simulations, using C(110) and C(110) surface facets in both bulk-terminated (top) and structurally optimized (bottom) configurations. In the bulk-terminated configuration shown in the top image, there are fringing fields at and near the corners, but the two facets have the same potential in vacuum. This indicates that the effects seen at the nanowire corners in Fig. 4 may be locally restricted. The simulation shown in the bottom image, with structurally optimized atom positions, has fewer fringing fields at the corners than the bulk-terminated simulation. This suggests that fringing-field-suppression might happen for some systems, which could modify expected mean inner potentials. Thus, optimized atom positions can influence the fringing fields around our simulated nanowires.

The nanowire simulation results are not used here to simulate a specific numerical value for V_0 . As noted above, the mean inner potential is calculated as a difference between two points: a point inside the material and a reference point far outside the material. The fringing fields visible in all cases in both Figs. 4 and 5 mean that the mean inner potential cannot be calculated, because no

unambiguous reference point is available. This is more obvious in Fig. 4, where the two facets differ by about 1.5 V; however, even in Fig. 5, there are external fringing fields around the corners. This result is not seen in the thin-film systems from the previous sections; only in the nanowire system, where it is possible to have corners, can this result be obtained. Thus, these simulations' most salient features for this work are the presence of fringing fields and the different mean inner potentials down the different facets; we present them on that basis, and not for exact V_0 values for these nanowires.

Our nanowire simulations show that including multiple surface facets creates fringing fields, which can be modified by structural optimization. Including different bulk-terminated surface facets with different thin-film mean inner potentials can lead to differences in the electrostatic potential in vacuum outside the nanowire, but the magnitude of this shift is not necessarily the same as that predicted from the independent thin-film simulations. Thus, linking multiple surface facets in the same DFT simulation can lead to a different mean inner potential than those facets taken individually. In the next section, we discuss the implications of all these surface-dependent results for the mean inner potential.

3. Discussion

Section 2 details many different DFT simulations, summarized and discussed in this section. First, we have established that our DFT simulations yield mean inner potentials in line with other DFT codes for group-IV and group-III-V materials. Second, we have also established precision limits for our DFT simulations, allowing us to evaluate whether changing a particular parameter influences the mean inner potential. Then, we performed thin-film mean inner potential calculations under different surface conditions, using our precision limits to decide if a surface condition changed the mean inner potential. These surface conditions included different bulk-terminated surface facets, with and without structural optimization or reconstruction (using minimum-energy lattice parameters to avoid pre-strained systems), and different adsorbate species. Finally, we performed nanowire mean inner potential calculations to examine the effects of including multiple surface facets in a single simulation.

In Section 3.1, we evaluate what kinds of surface-dependent V_0 shifts we have simulated. In Section 3.2, we discuss the theoretical basis for a surface-dependent V_0 . Finally, in Section 3.3, we discuss how our results can inform and influence mean inner potential measurements.

3.1. Summary of DFT MIP results

The accuracy and precision of our DFT-simulated mean inner potentials are comparable to other DFT simulations reported in the literature. The GPAW DFT code determines mean inner potentials with about the same precision as WIEN2k as used by Kruse et al. [14]. When tested for the same materials and surfaces, Table 2 shows that the mean inner potentials determined by GPAW are very close to those in previous DFT reports, with the exception of GaP due to a difference in lattice parameter. By using a different DFT program to confirm these previous simulation results, we show that different DFT programs can yield similar mean inner potentials.

According to our simulations, the mean inner potential can be strongly dependent on the surface condition. In Table 8, we compile the results from Tables 2 and 4–7 for Si only, with both a_d and a_r lattice parameters – the rest of this section discusses the results across all materials, not just silicon. Not every plausible and realistic surface configuration was tested, but enough surface

Table 8

Summary of DFT-simulated V_0 values for silicon simulations only. The values in this table are duplicates of those elsewhere in this paper; they are consolidated here for ease of comparison. Table indicates which table in this paper the value is cross-listed from. Facet indicates crystal surface facet – (2 × 1) indicates that surface reconstruction; otherwise, (1 × 1) surface reconstructions were used. Relax? indicates relaxed – Op indicates optimized from bulk-lattice starting positions; OR indicates optimized from experimental starting positions, R indicates reference atom positions but not DFT-position-optimized. Adsorbate indicates adsorbate – H/H is both surfaces covered with hydrogen. As in the other tables, $\Delta_{(110)}$ (V) is the V_0 shift from the baseline (110) bulk-terminated value, and is boldfaced if this value is outside the mutual margin of error.

Table	Facet	Relax?	Adsorbate	V_0 (V)	$\Delta_{(110)}$ (V)
$a = a_r$					
2	(110)	–	–	12.59 ± 0.05	Baseline
5	(001)	–	–	12.90 ± 0.05	+0.31
5	(111)	–	–	12.65 ± 0.05	+0.06
5	(211)	–	–	12.57 ± 0.05	–0.02
$a = a_d$					
4	(110)	–	–	12.32 ± 0.05	Baseline
5	(001)	–	–	12.85 ± 0.05	+0.54
5	(111)	–	–	12.37 ± 0.05	+0.06
5	(211)	–	–	12.29 ± 0.05	–0.03
6	(110)	Op	–	12.16 ± 0.05	–0.15
6	(001)	Op	–	12.90 ± 0.05	+0.59
6	(001)(2 × 1)	R	–	12.02 ± 0.05	–0.30
6	(001)(2 × 1)	OR	–	12.14 ± 0.05	–0.18
7	(001)(2 × 1)	R	H/H	11.52 ± 0.05	–0.80
7	(001)(2 × 1)	OR	H/H	11.52 ± 0.05	–0.80
7	(110)	Op	H/H	11.33 ± 0.05	–0.99
7	(110)	Op	O/O	15.73 ± 0.05	+3.41
7	(110)	Op	C/C	11.86 ± 0.05	–0.46
7	(110)	Op	Ge/Ge	12.83 ± 0.05	+0.51

configurations were tested to allow some conclusions to be drawn. Compared to bulk-terminated (110) surface DFT calculations, in our results, there was a V_0 shift in 10 of 18 simulations with different bulk-terminated surface facets, 14 of 16 clean reconstructed surfaces, and 16 of 16 reconstructed adsorbate-covered surfaces. For surface reconstructions, both experimental atom positions and *ab initio* structural optimization yielded V_0 shifts. The largest and most consistent V_0 shift was seen for adsorbate-covered surfaces. However, in most simulations, modifying the specimen surface shifted V_0 . Thus, according to our DFT simulations of the mean inner potential, the mean inner potential can be dependent on the surface facet, specimen surface reconstruction, and adsorbate state.

While DFT simulations are still approximations, they are widely applied to solve many electronic structure problems [31], and are more realistic than an ensemble of isolated, non-bonding atoms. Isolated-atom-scattering-factor (IASF) mean inner potentials are often, but not always, greater than clean-surface DFT-simulated mean inner potentials – to give one example, in Table 5, for C(001) and C(111), $V_{0,IASF} < V_{0,DFT}$. Kruse et al. [14] conclude that the IASF method overestimates V_0 by 10% compared to DFT simulations due to bonding and DFT effects, but that conclusion is based on only (110) bulk-terminated-surface DFT simulations. Our results show that the IASF method misestimates V_0 compared to DFT simulations, but this misestimation is surface-dependent in both magnitude and sign. Theoretically, IASF simulations only have one possible surface state, while DFT simulations can simulate different surface states. In short, DFT is more realistic than conventional IASF calculations, but, because DFT simulations show that specific surface state conditions influence the mean inner potential, then there is no general surface-independent conversion factor between IASF results and realistic DFT results.

The nanowire simulations provide additional insight into this surface dependence. The thin-film simulations show that the

mean inner potential is surface-facet-dependent, while the nanowire simulations show that the specific surface facet combinations can influence the mean inner potential. From the thin-film simulations, 1.05 V of V_0 shift between bulk-terminated C(001) and C(110) is expected; the nanowire simulations show that the difference outside these two facets is closer to 1.5 V when they are included in the same simulation. Computational restrictions and fringing fields mean that the nanowire simulations seen here cannot be used to calculate V_0 ; it might be possible for larger simulations with fewer fringing fields. These simulations all have noticeable fringing fields; as a result, no unambiguous mean inner potential could be calculated from these simulations. Thus, the nanowire simulations reinforce the conclusions of the thin-film simulations – that the exact surface configuration matters for the mean inner potential.

This surface-dependent effect should be seen for bulk mean inner potentials. We reiterate that, as discussed in Section 2.3, these V_0 simulations are performed by subtracting the average potential between two volumes – the middle of the vacuum and the middle of the thin film. These two volumes are sufficiently far from the surfaces to allow this to be a bulk-like V_0 , as shown in Fig. 3c and d. The surface atoms themselves are not included in either volume. For an experimental V_0 measurement from a thick specimen, the bulk-like V_0 is responsible for the vast majority of the measured phase shift, with deviations only in a few-nanometer layer at the top and bottom surfaces predicted in Fig. 3c. The theoretical reason for this surface effect on a bulk-like property is discussed in the next section.

3.2. Theoretical MIP surface dependence

A mean inner potential surface dependence was theoretically predicted by Saldin and Spence [38], summarized in their Eq. (18):

$$|e|V_0 + |e|V_{xc}(\epsilon_F) = \epsilon_F + \Phi \quad (1)$$

where $|e|$ is the electron charge, V_0 is the mean inner potential, Φ is the work function, ϵ_F is the Fermi-level energy, and $V_{xc}(\epsilon_F)$ is the exchange–correlation potential of an electron at the Fermi level. Saldin and Spence note that Eq. (1) holds for high energies, where the beam electron does not correlate with the specimen electrons; the low-energy equivalent would not contain $V_{xc}(\epsilon_F)$ [38]. According to Eq. (1), Φ makes V_0 surface-dependent, even in the bulk of a material. This is a necessary consequence of the electrostatic potential being measured between the interior and the exterior of the material [15]. While it is not explicitly mentioned in previous work, Φ includes exchange–correlation effects [47] that will not be present for a high-energy electron.

Φ -shifts may predict and partially explain V_0 -shifts. DFT simulations of the work function of both thin-film and nanowire Al specimens, including structural optimization, reported that both surface facet and structural optimization influenced the work function [48–50]. Experimentally, the work function is surface-dependent: for p-doped Si(001), $\Phi = 4.91$ V, and for p-doped Si(111), $\Phi = 4.60$ V [51]. This +0.31 V Φ shift compares favorably to the 0.25 V V_0 shift between the Si(001) [12.90 ± 0.05 V] and Si(111) [12.65 ± 0.05 V] bulk-terminated surfaces seen in Table 5. We also note that hydrogenating diamond C(001) surfaces can decrease their work function, as we have seen for the mean inner potential [52]. However, a V_0 measurement, unlike a Φ measurement, excludes exchange and correlation effects between the specimen and the measurement electron, so V_0 shifts may be similar but not identical to Φ shifts. While clean, bulk-terminated surfaces may not be realistic, and while work functions include some exchange and correlation effects not included in V_0 measurements, they still provide a baseline for comparison. Assuming no Fermi-level

effects, a pair of specimens that have different work functions is theoretically predicted to have different mean inner potentials.

We note here in passing that Φ has both band-bending and electron-affinity components, and both are surface-dependent [47]. Band bending has been discussed for observed p–n junction “inactive thickness” effects measured using electron holography [53,54], but those experimental maps of the electrostatic potential across a p–n junction assume that the mean inner potential does not change across the junction. However, one possible theoretical explanation for this effect could be a band-bending shift, leading to a Φ -shift, leading to a surface-dependent V_0 shift measured on a bulk specimen. Thus, band bending and electron affinity can possibly be explored using electron holography.

We also note that, according to Eq. (1), V_0 can also shift due to changes in the Fermi level ϵ_F , potentially explaining our nanowire results. This is possibly relevant for Fermi-level pinning effects through either dopants or adsorbed layers [47], so, in those situations, the interaction between ϵ_F and Φ should be considered. We note that the p–n junction band bending discussed above has been linked with Fermi-level pinning, based on tomographic results [55]. This ϵ_F shift may explain the V_0 mismatch between the C(001)/C(110) nanowire (~ 1.5 V) and respective thin-films (1.05 V).

In addition, if Φ , ϵ_F , and V_0 were all measured accurately and precisely, exchange-correlation effects could be measured directly. This could be of interest for future density functional theory simulations, to help improve their exchange-correlation functionals.

In summary, the mean inner potential has been theoretically predicted to be surface-dependent. That prediction links the mean inner potential to the work function and the Fermi level, and helps explain why our DFT simulations show a surface-dependent V_0 .

3.3. Experimental MIP measurements

Now, we consider how surface-dependent mean inner potentials affect experimental measurements. Surface dependence is a possible cause for the large variance in experimental V_0 measurements. The challenge, if the mean inner potential is surface dependent, is to figure out how to control, model, and replicate TEM specimen surfaces. The corresponding opportunity is surface-sensitive measurements using electron holography, which would depend on several factors.

Adsorbate-covered surfaces may explain the variance in experimentally measured mean inner potentials. As listed in Section 1, multiple V_0 measurements on the same material often do not agree, but these measurements are often on different specimen types. Section 1 lists two different methods for germanium preparation, and, for silicon, (111) and (110) cleaved wedges, oxide-covered nanospheres, and crushed bulk Si. Based on our simulation results, it is not implausible that at least some of the specimens used had different actual mean inner potentials. Our simulations have shown that different specimen surfaces can influence the mean inner potential by approximately 30% in some cases (Table 7), which could explain much of this variance. If specimens of the same material were prepared under different conditions and were not subjected to rigorous surface control, or if they contaminated differently in the TEM, then different specimens of the same material might have different mean inner potentials. Unlike charging or dynamical diffraction, which are dependent on beam condition and crystal orientation [19,17], these surface-dependent effects would affect any measurement of the mean inner potential, no matter how careful, and could easily lead to variations in experimental V_0 measurements. For a given specimen, DFT V_0 simulations of plausible surface states could diagnose if the mean inner potential variance is due to surface effects.

Our results indicate that V_0 is predicted to be surface-sensitive, but other specimen surface configurations could have different V_0

shifts. The surface configurations in this work were chosen to provide a systematic, multi-specimen, multi-material overview of possible V_0 surface effects, including experimental data where available. Thus, not all surfaces simulated here may be experimentally accessible in the TEM, and some experimentally accessible surfaces for these materials have not been simulated in this work. However, our simulation results do indicate that, for V_0 measurements, DFT simulations that include the effects of different plausible surfaces could improve V_0 measurement reliability.

The TEM electron beam may lead to different surface conditions than those simulated using DFT. Even a pre-prepared, known specimen surface might change during electron irradiation due to radiation damage. Additionally, electron-beam-induced charging may modify the electronic structure of the material. However, as shown in the nanowire simulations in Figs. 4 and 5, even an uncharged specimen could, in principle, generate fringing fields, although these could be suppressed by surface atom rearrangement as in Fig. 5. These fringing fields might have long-range effects, and thus which specimen facet is normal to the beam might change the measured mean inner potential. Thus, a TEM specimen surface may have a different atomic and electronic structure *in situ*, and determining this structure may require both measurements and simulations.

This surface-sensitivity for V_0 presents opportunities for electron holography. Taking a single specimen and modifying the specimen surface *in situ* could yield V_0 shifts without changing the specimen thickness, according to our DFT simulations. Because the electron holographic phase shift is proportional to the thickness and mean inner potential [3], a thicker specimen could yield a more precise surface-sensitive measurement. In principle, this could be used to quantitatively identify different specimen surface terminations using electron holography. However, identifying specific surface terminations would only be plausible when combined with DFT simulations of the range of expected or plausible surface conditions. As the nanowire simulations show, the DFT simulations can also include not just realistic surfaces, but multi-surface specimens, which could yield better specimen knowledge. An ultra-high-vacuum TEM might help achieve this level of specimen surface stability.

4. Conclusions

In this work, we have extensively examined and quantified surface effects on the mean inner potential (V_0) using density functional theory (DFT). According to our set of DFT simulations, different DFT codes return similar V_0 values, and V_0 is found to be dependent on surface facet, surface termination, and adsorbate state. In addition, “nanowire” simulations show that multi-surface DFT simulations may yield different V_0 results than single-surface “thin-film” measurements. This surface dependence of the mean inner potential, predicted from both theory and simulation for even bulk-like specimens, could explain the reported variance in mean inner potential experimental measurements.

Future work could examine the mean inner potential's surface dependence for more systems, both experimentally and in simulation. These surface-dependent DFT simulations could also be combined with image simulations, potentially aiding in retrieval of crystal properties like strain and ferroelectric polarization [56–58], or of atomic positions [59]. Hardware-accelerated image simulations may be fast enough to efficiently combine with DFT simulations [60,61], which offers the mean inner potential as another method for benchmarking DFT simulation accuracy [35]. Experiments could include modification of the atomic structure of TEM specimen surfaces or careful TEM specimen preparation under surface-controlling conditions.

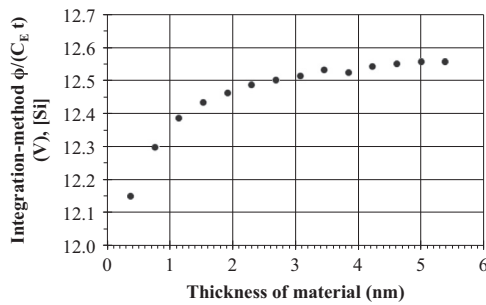


Fig. B1. “Integration-method” V_0 from the thin-film Si specimens in Fig. 3c, corresponding to the expected ideal measurements for these particular thin films. However, these values are not applicable to a general V_0 measurement.

Acknowledgments

This paper is based on and includes research comprising part of R.S.P.’s doctoral thesis, performed and presented at the Center for Electron Nanoscopy, Technical University of Denmark. R.S.P. acknowledges funding from the Technical University of Denmark and from the German Research Foundation (DFG) under Grant no. KO 2911/7-1.

Appendix A. Exchange-correlation functional

While it is possible to choose between different exchange-correlation functionals in GPAW, this is not included in our precision testing, because a different exchange-correlation functional means a different approximate electron–electron interaction model, and thus a different physical system [31]. Different exchange-correlation functionals are used for different systems, and the PBE functional [37] we use is a common choice, in part because the generalized-gradient approximation it uses is viewed as more accurate than the local-density approximation, and other similar functionals have been based on PBE but designed for specific purposes [31,62,37]. Calculations using the LDA [31], revPBE [63] and RPBE [62] functionals for diamond C yielded V_0 values of 20.38 V, 20.35 V, and 20.39 V, respectively; for Si, the same functionals yielded 12.54 V, 12.59 V, and 12.62 V, respectively. The exchange-correlation functional is an approximation, and multiple choices are available; however, as long as a single exchange-correlation functional is consistently applied, the electron–electron interaction model should be consistent.

Appendix B. Measuring mean inner potentials from thin specimens

This appendix briefly discusses measuring V_0 for thin specimens. V_0 is usually measured for thick specimens because the measured phase shift ϕ goes as $\phi = C_E V_0 t$ (C_E a voltage-dependent constant and t the specimen thickness), but V_0 has been occasionally measured for thin specimens [29]. Thin specimens include the substantial challenge of thickness determination – while $\pm 1\%$ thickness precision for a 100 nm specimen is 1 nm, $\pm 1\%$ for a 2 nm specimen is 0.02 nm (0.2 Å), and V_0 precision depends on thickness precision. For a thick specimen, integrating over the surface layers will cause only a slight shift to V_0 , perhaps comparable to the thickness imprecision. However, for a thin specimen, the percentage of the thickness that is within a few layers of the surface will be higher, so the expected V_0 measurement will be distorted from the expected bulk value. Thus, an “integration method” $\phi/(C_E t)$ that integrates along the entire thickness can be

considered for thin specimens and contrasted with the “subtraction method” V_0 used in the rest of the text. It is extremely important to note that the integration method results *only* apply to that exact thickness, unlike the thickness-independent subtraction method. In Fig. B1, we show the result of the integration method for the same specimens as in Fig. 3c. Compared to Fig. 3c, the integration method takes much longer to stabilize, because it directly includes the surface layers in its integration volume, and Fig. 3c shows that the layers near the surface have lower potentials compared to the bulk-like deeper layers, where V_0 has stabilized. Thus, while the integration method is potentially interesting for comparison with measurements of thin specimens, it is much less useful for general thickness-independent calculation.

References

- [1] D. Gabor, A new microscopic principle, *Nature* 161 (4098) (1948) 777–778.
- [2] G. Möllenstedt, H. Düker, Beobachtungen und Messungen an Biprisma-Interferenzen mit Elektronenwellen, *Z. Phys.* 145 (3) (1956) 377–397.
- [3] E. Völkl, L.F. Allard, D.C. Joy (Eds.), *Introduction to Electron Holography*, Plenum Press, New York, 1998.
- [4] R. Buhl, Interferenzmikroskopie mit Elektronenwellen, *Z. Phys.* 155 (4) (1959) 395–412.
- [5] A. Tonomura, Electron-holographic interference microscopy, *Adv. Phys.* 41 (1992) 59–103.
- [6] J.K. Weiss, W.J. de Ruijter, M. Gajdardziska-Josifovska, M.R. McCartney, D. J. Smith, Applications of electron holography to the study of interfaces, *Ultramicroscopy* 50 (3) (1993) 301–311.
- [7] W.D. Rau, P. Schwander, F.H. Baumann, W. Höppner, A. Ourmazd, Two-dimensional mapping of the electrostatic potential in transistors by electron holography, *Phys. Rev. Lett.* 82 (12) (1999) 2614–2617.
- [8] A.C. Twitchett, R.E. Dunin-Borkowski, R.F. Broom, P.A. Midgley, Quantitative electron holography of biased semiconductor devices, *J. Phys.: Condens. Matter* 16 (2003) S181–S192.
- [9] P.A. Midgley, R.E. Dunin-Borkowski, Electron tomography and holography in materials science, *Nat. Mater.* 8 (2009) 271–280.
- [10] M.R. McCartney, N. Agarwal, S. Chung, D.A. Cullen, M.-G. Han, K. He, L. Li, H. Wang, L. Zhou, D.J. Smith, Quantitative phase imaging of nanoscale electrostatic and magnetic fields using off-axis electron holography, *Ultramicroscopy* 110 (5) (2010) 375–382.
- [11] J.A. Ibers, Atomic scattering amplitudes for electrons, *Acta Crystallogr.* 11 (3) (1958) 178–183.
- [12] P.A. Doyle, P.S. Turner, Relativistic Hartree–Fock X-ray and electron scattering factors, *Acta Crystallogr. A* 24 (3) (1968) 390–397.
- [13] M. O’Keeffe, J.C.H. Spence, On the average Coulomb potential ϕ_0 and constraints on the electron density in crystals, *Acta Crystallogr. A* 50 (1) (1994) 33–45.
- [14] P. Kruse, M. Schowalter, D. Lamoen, A. Rosenauer, D. Gerthsen, Determination of the mean inner potential in III–V semiconductors, Si and Ge by density functional theory and electron holography, *Ultramicroscopy* 106 (2) (2006) 105–113.
- [15] L. Kleinman, Comment on the average potential of a Wigner solid, *Phys. Rev. B* 24 (12) (1981) 7412–7414.
- [16] M.Y. Kim, J.M. Zuo, J.C.H. Spence, Ab-initio LDA calculations of the mean coulomb potential V_0 in slabs of crystalline Si, Ge and MgO, *Phys. Status Solidi A* 166 (1) (1998) 445–451.
- [17] R.S. Pennington, J.J. Mortensen, T. Kasama, C.B. Boothroyd, R.E. Dunin-Borkowski, Theoretical and experimental factors affecting measurements of semiconductor mean inner potentials, *J. Phys.: Conf. Ser.* 209 (2010) 012030.
- [18] G. Möllenstedt, M. Keller, Elektroneninterferometrische Messung des inneren Potentials, *Z. Phys.* 148 (1) (1957) 34–37.
- [19] M. Gajdardziska-Josifovska, M. McCartney, W.d. Ruijter, D. Smith, J. Weiss, J. Zuo, Accurate measurements of mean inner potential of crystal wedges using digital electron holograms, *Ultramicroscopy* 50 (3) (1993) 285–299.
- [20] Y.C. Wang, T.M. Chou, M. Libera, T.F. Kelly, Transmission electron holography of silicon nanospheres with surface oxide layers, *Appl. Phys. Lett.* 70 (1997) 1296.
- [21] L. Wu, M.A. Schofield, Y. Zhu, J. Taftø, A unique determination of boundary condition in quantitative electron diffraction: application to accurate measurements of mean inner potentials, *Ultramicroscopy* 98 (2–4) (2004) 135–143.
- [22] J. Li, M.R. McCartney, R.E. Dunin-Borkowski, D.J. Smith, Determination of mean inner potential of germanium using off-axis electron holography, *Acta Crystallogr. A* 55 (4) (1999) 652–658.
- [23] P. Kruse, A. Rosenauer, D. Gerthsen, Determination of the mean inner potential in III–V semiconductors by electron holography, *Ultramicroscopy* 96 (1) (2003) 11–16.
- [24] A. Goswami, N.D. Lisgarten, The measurement of the inner potential of diamond, *J. Phys. C: Solid State Phys.* 13 (8) (1980) 1381.
- [25] D.E. Ashenford, N.D. Lisgarten, The measurement of inner potential for

- diamond, germanium and silicon, *Acta Crystallogr. A* 39 (3) (1983) 311–314.
- [26] A. Goswami, N.D. Lisgarten, The measurement of inner potentials for copper, silver and gold, *J. Phys. C: Solid State Phys.* 15 (1982) 4217.
- [27] H. Hoffmann, C. Jönsson, Elektroneninterferometrische Bestimmung der mittleren inneren Potentiale von Al, Cu und Ge unter Verwendung eines neuen Präparationsverfahrens, *Z. Phys.* 182 (4) (1965) 360–365.
- [28] A. Lubk, D. Wolf, H. Lichte, The effect of dynamical scattering in off-axis holographic mean inner potential and inelastic mean free path measurements, *Ultramicroscopy* 110 (5) (2010) 438–446.
- [29] R. Popescu, E. Müller, M. Wanner, D. Gerthsen, M. Schowalter, A. Rosenauer, A. Böttcher, D. Löffler, P. Weis, Increase of the mean inner Coulomb potential in Au clusters induced by surface tension and its implication for electron scattering, *Phys. Rev. B* 76 (23) (2007) 235411.
- [30] D. Rez, P. Rez, I. Grant, Dirac–Fock calculations of X-ray scattering factors and contributions to the mean inner potential for electron scattering, *Acta Crystallogr. A* 50 (4) (1994) 481–497.
- [31] R.M. Martin, *Electronic Structure: Basic Theory and Practical Methods*, Cambridge University Press, Cambridge, UK, 2004.
- [32] M. Schowalter, A. Rosenauer, D. Lamoen, P. Kruse, D. Gerthsen, Ab initio computation of the mean inner Coulomb potential of Wurtzite-type semiconductors and gold, *Appl. Phys. Lett.* 88 (2006) 232108.
- [33] M. Schowalter, D. Lamoen, A. Rosenauer, P. Kruse, D. Gerthsen, First-principles calculations of the mean inner Coulomb potential for sphalerite type II–VI semiconductors, *Appl. Phys. Lett.* 85 (21) (2004) 4938–4940.
- [34] M. Schowalter, J.T. Titantah, D. Lamoen, P. Kruse, Ab initio computation of the mean inner Coulomb potential of amorphous carbon structures, *Appl. Phys. Lett.* 86 (2005) 112102.
- [35] J. Enkovaara, C. Rostgaard, J.J. Mortensen, J. Chen, M. Dułak, L. Ferrighi, J. Gavnholt, C. Glinsvad, V. Haikola, H.A. Hansen, H.H. Kristoffersen, M. Kuisma, A.H. Larsen, L. Lehtovaara, M. Ljungberg, O. Lopez-Acevedo, P.G. Moses, J. Ojanen, T. Olsen, V. Petzold, N.A. Romero, J. Stausholm-Møller, M. Strange, G. A. Tritsarlis, M. Vanin, M. Walter, B. Hammer, H. Häkkinen, G.K.H. Madsen, R. M. Nieminen, J.K. Nørskov, M. Puska, T.T. Rantala, J. Schiøtz, K.S. Thygesen, K. W. Jacobsen, Electronic structure calculations with GPAW: a real-space implementation of the projector augmented-wave method, *J. Phys.: Condens. Mater.* 22 (25) (2010) 253202.
- [36] J.J. Mortensen, L.B. Hansen, K.W. Jacobsen, Real-space grid implementation of the projector augmented wave method, *Phys. Rev. B* 71 (3) (2005) 35109.
- [37] J. Perdew, K. Burke, M. Ernzerhof, Generalized gradient approximation made simple, *Phys. Rev. Lett.* 77 (18) (1996) 3865–3868.
- [38] D.K. Saldin, J.C.H. Spence, On the mean inner potential in high- and low-energy electron diffraction, *Ultramicroscopy* 55 (4) (1994) 397–406.
- [39] K. Jakobsen, S.R. Bahn, An object-oriented scripting interface to a legacy electronic structure code, *Comput. Sci. Eng.* 4 (3) (2002) 56–66.
- [40] L.I. Berger, *CRC Handbook of Chemistry and Physics, Properties of Semiconductors*, 88th edition, CRC Press, Boca Raton, FL, 2007.
- [41] H.W. King, *CRC Handbook of Chemistry and Physics, Crystal Structures and Lattice Parameters of Allotropes of the Elements*, 89th edition, CRC Press, Boca Raton, FL, 2008.
- [42] M. Schowalter, A. Rosenauer, J.T. Titantah, D. Lamoen, Computation and parametrization of the temperature dependence of Debye–Waller factors for group IV, III–V and II–VI semiconductors, *Acta Crystallogr. A* 65 (1) (2008) 5–17.
- [43] S. Sque, R. Jones, P. Briddon, Structure, electronics, and interaction of hydrogen and oxygen on diamond surfaces, *Phys. Rev. B* 73 (8) (2006) 085313.
- [44] R. Stallcup, J. Perez, Atomic structure of steps and defects on the clean diamond (100)- 2×1 surface studied using ultrahigh vacuum scanning tunneling microscopy, *Appl. Phys. Lett.* 81 (24) (2002) 4538–4540.
- [45] H. Over, J. Wasserfall, W. Ranke, C. Ambiatello, R. Sawitzki, D. Wolf, W. Moritz, Surface atomic geometry of Si (001)- (2×1) : a low-energy electron-diffraction structure analysis, *Phys. Rev. B* 55 (7) (1997) 4731–4736.
- [46] E. Lauridsen, Structure determination of the Si (001)- (2×1) -H reconstruction by surface X-ray diffraction: weakening of the dimer bond by the addition of hydrogen, *Surf. Sci.* 453 (2000) 18–24.
- [47] A. Zangwill, *Physics at Surfaces*, Cambridge University Press, Cambridge, UK, 1988.
- [48] C. Fall, N. Binggeli, A. Baldereschi, Deriving accurate work functions from thin-slab calculations, *J. Phys.: Condens. Mater.* 11 (1999) 2689.
- [49] C. Fall, N. Binggeli, A. Baldereschi, Work functions and surface charges at metallic facet edges, *Phys. Rev. B* 66 (7) (2002) 075405.
- [50] C. Fall, N. Binggeli, A. Baldereschi, Work functions at facet edges, *Phys. Rev. Lett.* 88 (15) (2002) 156802.
- [51] D. Lide, *CRC Handbook of Chemistry and Physics, Electron Work Function of the Elements*, 90th edition, CRC Press, Boca Raton, FL, 2009.
- [52] G. Brandes, A. Mills, Work function and affinity changes associated with the structure of hydrogen-terminated diamond (100) surfaces, *Phys. Rev. B* 58 (8) (1998) 4952–4962.
- [53] D. Cooper, R. Truche, A.C. Twitchett-Harrison, R.E. Dunin-Borkowski, P. Midgley, Quantitative off-axis electron holography of GaAs p–n junctions prepared by focused ion beam milling, *J. Microsc.* 233 (1) (2009) 102–113.
- [54] D. Cooper, C. Ailliot, J.-P. Barnes, J.-M. Hartmann, P. Salles, G. Benassayag, R. E. Dunin-Borkowski, Dopant profiling of focused ion beam milled semiconductors using off-axis electron holography; reducing artifacts, extending detection limits and reducing the effects of gallium implantation, *Ultramicroscopy* 110 (5) (2010) 383–389.
- [55] D. Wolf, A. Lubk, A. Lenk, S. Sturm, H. Lichte, Tomographic investigation of fermi level pinning at focused ion beam milled semiconductor surfaces, *Appl. Phys. Lett.* 103 (26) (2013) 264104.
- [56] R.S. Pennington, W. Van den Broek, C.T. Koch, Third-dimension information retrieval from a single convergent-beam transmission electron diffraction pattern using an artificial neural network, *Phys. Rev. B* 89 (20) (2014) 205409.
- [57] R.S. Pennington, C.T. Koch, Retrieving depth-direction information from TEM diffraction data under reciprocal-space sampling variation, *Ultramicroscopy* 148 (2015) 105–114.
- [58] R.S. Pennington, C.T. Koch, A three-dimensional polarization domain retrieval method from electron diffraction data, *Ultramicroscopy* 155 (C) (2015) 42–48.
- [59] W. Van den Broek, C.T. Koch, Method for retrieval of the three-dimensional object potential by inversion of dynamical electron scattering, *Phys. Rev. Lett.* 109 (24) (2012) 245502.
- [60] C. Dwyer, Simulation of scanning transmission electron microscope images on desktop computers, *Ultramicroscopy* 110 (3) (2010) 195–198.
- [61] R.S. Pennington, F. Wang, C.T. Koch, Stacked-Bloch-wave electron diffraction simulations using GPU acceleration, *Ultramicroscopy* 141 (2014) 32–37.
- [62] B. Hammer, L.B. Hansen, J.K. Nørskov, Improved adsorption energetics within density-functional theory using revised Perdew–Burke–Ernzerhof functionals, *Phys. Rev. B* 59 (1999) 7413–7421.
- [63] Y. Zhang, W. Yang, Comment on “Generalized gradient approximation made simple”, *Phys. Rev. Lett.* 80 (1998) 890.